Macromolecules

pubs.acs.org/Macromolecules Article

Spherical Micelles with Nonspherical Cores: Effect of Chain Packing on the Micellar Shape

Nico König, Lutz Willner,* Göran Carlström, Thomas Zinn, Kenneth D. Knudsen, Frode Rise, Daniel Topgaard, and Reidar Lund*

Cite This: *Macromolecules* 2020, 53, 10686−10698

Read Online

ACCESS | Metrics & More | Article Recommendations | Supporting Information

ABSTRACT: Self-assembly of amphiphilic polymers into micelles is an archetypical example of a "self-confined" system due to the formation of micellar cores with dimensions of a few nanometers. In this work, we investigate the chain packing and resulting shape of C_n-PEOx micelles with semicrystalline cores using small/wide-angle X-ray scattering (SAXS/WAXS), contrast-variation small-angle neutron scattering (SANS), and nuclear magnetic resonance spectroscopy (NMR). Interestingly, the *n*-alkyl chains adopt a rotator-like conformation and pack into prolate ellipses (axial ratio $\epsilon \approx 0.5$) in the "crystalline" region and abruptly arrange into a more spheroidal shape ($\epsilon \approx 0.7$) above the melting point. We attribute the distorted spherical shape above the melting point to thermal fluctuations and intrinsic rigidity of the *n*-alkyl blocks. We also find evidence for a thin dehydrated PEO layer (≤1 nm) close to the micellar core. The results provide substantial insight into the interplay between crystallinity and molecular packing in confinement and the resulting overall micellar shape.

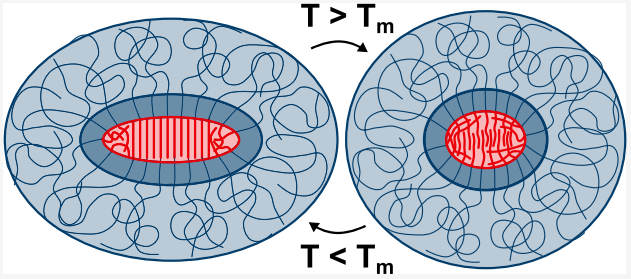

INTRODUCTION

The self-assembly of polymers and the resulting multitude of different nanostructures have found application in a range of fields.[1−3] Generally, association is driven by a reduction in the surface energy, in water notably by the hydrophobic effect.[4] However, other driving forces such as electrostatic interaction ("coacervation")[5] or crystallization may also be involved. The latter is being exploited to create novel nanostructures in crystallization-driven self-assembly (CDSA).[6−10] Crystallization, or at least packing into semiordered structures, is also important in more complex systems such as in the cell membrane.[11]

To better understand complex phenomena, it is customary to employ simpler, well-defined model systems. An excellent example is *n*-alkyl-functionalized poly(ethylene oxide) (C_n-PEOx) polymers, where the index n denotes the number of carbon atoms in the *n*-alkyl block and x the PEO molecular weight in kg/mol (compare Figure 1a). These polymers have been used as model materials to investigate fundamental properties of nonionic amphiphilic block copolymers. When dissolved in water, C_n-PEOx forms well-defined micellar entities. The highly hydrophobic, core-forming *n*-alkyl blocks represent the simplest hydrocarbons and are uniform ("monodisperse"). The hydrophilic, shell-forming PEO blocks, on the other hand, are chemically stable and are synthesized with very low polydispersities ($Đ < 1.05$) by sophisticated living polymerization techniques. Therefore, C_n-PEOx has been employed extensively to investigate phenomena like micellar aggregation behavior,[12−19] molecular exchange kinetics,[20−24] or macroscopic rheology.[25,26] A peculiar feature of C_n-PEOx with $n \geq 18$ is (partial) core crystallization below a certain temperature as observed via differential scanning calorimetry (DSC), nuclear magnetic resonance spectroscopy (NMR), and density measurements,[27−29] which may affect micellar structures and properties. For instance, Plazzotta et al. found that core freezing lead to segregation in a mixture of C_{18}-PEO1 and C_{18}-PEO5, even though the core blocks were identical.[30] The same group later exploited core freezing to trigger the release of a hydrophobic cargo from the micellar core.[31] However, the exact nature of the crystalline phase and how optimal packing is achieved in a confined state within a nanometer-sized micellar core are still open questions, in particular, how the conformational and spatial order affects the overall morphology of the micelles.

We recently reported on the effect of core crystallization on the molecular exchange kinetics between C_n-PEOx micelles.[21,23] Surprisingly, the effect is rather straightforward: In crystalline samples, the melting enthalpy is simply added to the thermal (hydrophobic) activation energy of the respective

Received: August 21, 2020
Revised: October 23, 2020
Published: November 18, 2020

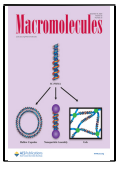

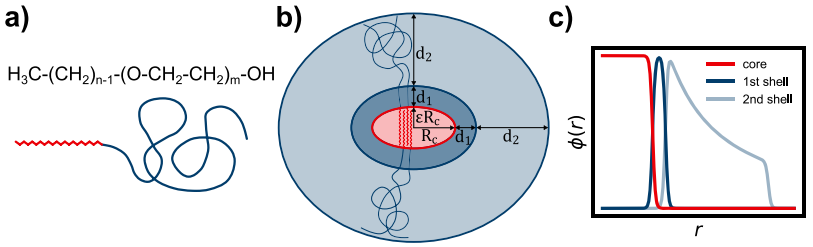

Figure 1. (a) Chemical structure of C_n-PEOx. (b) Sketch to illustrate the scattering model. (c) Sketch of the local polymer volume fraction assumed in the model.

molten sample, and the melting enthalpy can easily be tuned by coassembling C_n-PEOx with different n-alkyl block lengths.[19] However, it is not yet clear what kind of order the n-alkyl chains adopt in the crystalline core. In bulk crystalline phases, n-alkane molecules align in parallel and arrange in an all-trans conformation. In addition, there is a second solid-like phase before the actual melting transition, the so-called rotator phase. Here, the n-alkane molecules retain their parallel orientation but gain a rotational degree of freedom around the longitudinal axis.[32] Both phases are suitable candidates for the state of the C_n-PEOx n-alkyl blocks in solidified micellar cores. However, in our previous works where the structure of C_n-PEOx micelles was examined, we assumed that the core was spherical even though it is unclear how crystallized, all-trans n-alkyl chains can arrange in a spherical domain.

In the present paper, we address this issue using scattering techniques in combination with NMR spectroscopy. Wide-angle X-ray scattering (WAXS) yields information about the spatial order of the n-alkyl chains in both molten and crystalline condition within the micellar cores. We use small-angle neutron scattering (SANS) with contrast matching and detailed modeling of micellar form factors to determine the shape of the core. In addition, line width analysis of regular ^{1}H solution NMR spectra gives an idea about the general chain mobility while ^{13}C solid-state NMR (ssNMR) reveals further details: ^{13}C chemical shifts indicate the n-alkyl isomerization, all-trans vs trans-gauche. In the liquid phase, overall anisotropy and the rate of CH bond reorientation are quantified by the order parameter S_{CH}, whereas in the solid phase the dispersion of the relaxation rate in the rotating frame $R_{1\rho}$ sheds light on the correlation time τ_c.

EXPERIMENTAL SECTION

Synthesis. The C_n-PEOx polymers were prepared via ring-opening living anionic polymerization of ethylene oxide (EO) in toluene. Details of the synthesis were extensively presented in previous articles.[15,33] Besides the ordinary proteated C_n-hPEOx, deuterated and partly deuterated polymers were synthesized following the same protocol. Fully deuterated C_{22}-dPEO5 was prepared from d-EO and partly deuterated C_{28}-dhPEO5 from a 82/18 molar mixture of d- and h-EO, leading to a random distribution of monomers along the PEO chains.

The polymers were characterized by size-exclusion chromatography (SEC) using a multidetector chromatographic setup consisting of an autosampler, an isocratic pump (both Agilent Technologies, Series 1260 infinity), a column oven (Shimadzu CTO-20A), a refractive index (RI) detector (Optilab rEX), and an 18 angle light scattering detector (DAWN HELEOS-II), both detectors from Wyatt Technologies, for absolute molar mass determination. The polydispersities were determined to be $Đ \leq 1.04$ for all polymers. As a consistency check, M_n of the proteated polymers was additionally calculated from ^{1}H NMR spectra measured in deuterochloroform. The polymer characteristics are specified in Table 1.

Table 1. Polymer Characteristics

polymer[a]	N_{PEO}[b]	M_n[b] (g/mol)	M_n[c] (g/mol)	M_w[c] (g/mol)	M_w/M_n[c]
C_{28}-dhPEO5[d]	102	5240	5130	5260	1.03
C_{28}-hPEO3[e]	53	2750	2670	2780	1.04
C_{28}-hPEO5[e,f]	110	5250	5240	5150	1.02
C_{22}-dPEO5[g]	118		5980	6100	1.02
hPEO5[e,g,h]			5000[i]		
hPEO3[e,h]			3000[i]		

[a]h: proteated; d: deuterated; dh: partially deuterated. [b]From NMR. [c]From SEC. [d]Used in SAS experiments. [e]Used in WAXS experiments. [f]Used in ^{13}C NMR experiments. [g]Used in ^{1}H NMR experiments. [h]Commercial product of Sigma-Aldrich. [i]Supplier specification.

Sample Preparation. For all samples in this work, dry polymer powder was dissolved in H_2O or D_2O. Ultrapure H_2O (18.2 MΩ cm) was taken from a Millipore water purification system, and D_2O with 99.90% D was purchased from Eurisotop, France. To ensure well-equilibrated, homogeneous samples, the solutions were shaken for at least 1 h at 70 °C, well above all relevant melting points, and then left to cool overnight at room temperature while still being shaken. For SANS measurements, C_{28}-dhPEO5 with 82% dEO content was dissolved in D_2O, which is very close to the dhPEO match point. Volume fractions of ϕ = 0.5 and 4 vol % were prepared and used also for SAXS to ensure consistent measurements of the two complementary methods. For the WAXS study, the polymers were dissolved in H_2O at volume fractions of ϕ = 5 vol %. ^{1}H NMR spectra of C_{22}-dPEO5 were recorded in D_2O at ϕ = 0.5 vol %. Traces of 3-(trimethylsilyl)-2,2,3,3-tetradeuteropropionic acid (TMSP-d_4, Sigma-Aldrich) were added to calibrate the chemical shifts. For comparison, a measurement in deuterochloroform was done at a similar concentration. Solid-state ^{13}C NMR experiments were performed on a 50 vol % gel sample prepared from C_{28}-hPEO5 in D_2O. The gel was obtained by directly dissolving the polymer powder in D_2O. Homogenization was achieved by several heating (to 70 °C) and centrifugation cycles—in between turning the vial upside down. In a previous work we could successfully demonstrate that this procedure leads to micelles identical with those at low volume fractions.[33] The transparent gel was then transferred into a disposable magic angle spinning (MAS) insert purchased from Bruker.

Small-Angle Neutron Scattering. Small-angle neutron scattering (SANS) experiments on C_{28}-dhPEO5 in D_2O were performed at the time-of-flight instrument Sans2d at the STFC ISIS Neutron and Muon Source in Didcot, United Kingdom,[34,35] using neutron wavelengths λ = 2−14 Å. At a detector distance of 4 m, this allowed to cover a Q range of about 0.004−0.7 Å^{-1}, where $Q = 4\pi \sin(2\theta/2)/\lambda$ is the scattering vector and 2θ is the scattering angle. The collection time was 50 min per sample and temperature. To follow the structural evolution of the core during melting, measurements were done between 40 and 70 °C, well below and above the melting temperature of T_m = 57 °C. The scattering patterns were reduced and background-corrected according to instrument standard procedures. To avoid structure factor contributions, measurements were done in dilute solution at 0.25 vol %. Complementarily, a 4 vol % sample was measured to improve the scattering statistics at high Q, where the

https://dx.doi.org/10.1021/acs.macromol.0c01936
Macromolecules 2020, 53, 10686−10698

structure factor contribution is negligible. Both data sets were normalized by concentration—which yielded a perfect overlap at intermediate Q—and then combined to obtain the pure form factor with high signal-to-noise ratio over the entire Q range.

Small-Angle X-ray Scattering (SAXS). SAXS experiments were performed at the in-house Bruker NanoStar instrument at the Norwegian Centre for X-ray Diffraction, Scattering and Imaging (RECX) at the University of Oslo, Norway, using Cu Kα radiation of λ = 1.54 Å. The instrument covers a Q range of 0.009−0.3 Å^{-1}, and the collection time was 60 min. The exact same samples from the SANS beamtime were measured at both 40 and 70 °C to provide reference scattering patterns with PEO contribution, both below and above the core melting transition. Data reduction and background correction were performed according to instrument standard procedures, and the high- and low-concentration measurements were combined in the same way as for the SANS measurements.

Wide-Angle X-ray Scattering (WAXS). WAXS experiments were performed at beamline ID02 (ESRF, France) using an X-ray energy of 12.46 keV (wavelength λ = 0.995 Å). The WAXS detector (Rayonix LX-170HS) permits to cover a Q range of approximately 0.5 Å^{-1} < Q < 5.0 Å^{-1}.

^{1}H Nuclear Magnetic Resonance Spectroscopy. Conventional solution proton nuclear magnetic resonance spectroscopy (^{1}H NMR) was performed at the University of Oslo NMR Center using a Bruker Avance I 600 MHz NMR spectrometer equipped with a TCI cryo probe. The program Topspin 2.1 (patch level 6) was used for both acquisition and processing. C_{22}-dPEO5 samples dissolved in D_2O and $CDCl_3$ at ∼0.5 vol % were measured in standard 5 mm NMR tubes in a temperature range T = 10−50 °C (T_m = 29 °C). In D_2O, minute amounts of TMSP-d_4 were used to calibrate the chemical shifts, whereas in deuterochloroform the residual $CHCl_3$ signal at 7.24 ppm was used. After the set temperature was reached, the spectrometer was shimmed and the sample left to equilibrate for 10 min before a second round of shimming as well as tuning and matching were performed, followed by the actual measurement. To suppress the residual H_2O signal, an excitation sculpting (pulse program: zgesgp) suppression scheme[36] was employed.

^{13}C Solid-State Nuclear Magnetic Resonance Spectroscopy. Magic angle spinning (MAS) solid-state carbon nuclear magnetic resonance spectroscopy (^{13}C ssNMR) was performed at the NMR Center of Lund University using a Bruker Avance Neo 500 MHz NMR spectrometer equipped with a Bruker 4 mm HCP E-free MAS probe. Topspin 4.0 (patchlevel 7) was used for both acquisition and processing. An ∼50 vol % C_{28}-hPEO5 gel in D_2O was filled into disposable MAS inserts (Bruker) in a 4 mm rotor and spun at 4−6 kHz.

First, polarization transfer experiments using cross-polarization (CP)[37] and refocused insensitive nuclei enhanced by polarization transfer (refocused-INEPT)[38,39] were performed at T = 41−74 °C. A spin rate of 6 kHz was applied to assess the CH bond reorientation of the n-alkyl and PEO blocks around the melting transition of the core (T_m = 57 °C). Prior to the measurement, the sample was heated to 76 °C for equilibration and then cooled again to 40 °C. Afterward, the temperature was increased stepwise with 5 min equilibration time before the start of each experiment.

Second, the longitudinal relaxation rate R_1 and the relaxation rate in the rotating frame $R_{1\rho}$ of ^{13}C were determined below the melting transition, T = 41−55 °C, revealing details about the CH bond reorientation correlation time τ_c in the solid phase. The experiments used CP polarization transfer and a MAS spin rate of 6 kHz. R_1 was measured with the inversion recovery method of Torchia,[40] and $R_{1\rho}$ was measured using an on-resonance spin-lock, applied to ^{13}C after CP.

Third, R-type proton detected local field (R-PDLF) experiments[41] were performed just above the melting transition, T = 57−77 °C, using refocused-INEPT polarization transfer and a spin rate of 4 kHz, to determine the liquid order parameter S_{CH} of CH bonds in the n-alkyl block:

$$S_{CH} = \frac{1}{2}\langle 3\cos^2\theta - 1\rangle \tag{1}$$

where θ is the angle between a ^{13}C−^{1}H internuclear vector and the magnetic field.

More details about the ^{13}C NMR experiments can be found in the Supporting Information.

SCATTERING MODEL

In previous publications, we used a spherical core−shell model to describe scattering data from C_n-PEOx micelles.[15,19,23,29] This model, however, fails in describing the SANS data with dominant core scattering contribution due to deviation from spherical shape and a dehydrated corona layer as outlined below.

Figure 1b shows a sketch of a newly developed, aspherical scattering model, including the important geometrical parameters. The micellar core is modeled as a homogeneous ellipsoid of revolution with an equatorial radius R_c and polar radius ϵR_c. Thus, ϵ < 1 corresponds to an oblate and ϵ > 1 to a prolate shape. The general scattering amplitude for such an ellipsoid of revolution is given by[42]

$$A_{el}(Q, R_{eff}) = 3\frac{\sin(QR_{eff}) - QR_{eff}\cos(QR_{eff})}{(QR_{eff})^3} \tag{2}$$

where R_{eff} is an effective radius depending on the equatorial radius R as well as the angle α between the axis of the ellipsoid and the scattering vector $\vec{Q}$:

$$R_{eff}(R, \alpha) = R\sqrt{\sin^2\alpha + \epsilon^2\cos^2\alpha} \tag{3}$$

Thus, with the effective core radius $R_{c,eff} = R_{eff}(R_c,\alpha)$, the core scattering amplitude is

$$A_c(Q, \alpha) = A_{el}(Q, R_{c,eff})e^{-Q^2\sigma_{int1}^2/2} \tag{4}$$

It contains a Debye−Waller factor accounting for an interface roughness σ_{int1} between core and first shell. The first shell of dehydrated polymer is assumed to be homogeneous and of constant thickness d_1 around the ellipsoidal core, so that the scattering amplitude is

$$A_{s1}(Q, \alpha) = \frac{1}{V_{s1}}\{[V_c + V_{s1}]A_{el}(Q, R_{s1,eff}) - V_cA_c(Q, \alpha)\}e^{-Q^2\sigma_{int2}^2/2} \tag{5}$$

with the effective inner and outer radii $R_{c,eff}$ and $R_{s1,eff} = R_{c,eff} + d_1$, another Debye−Waller factor with interface roughness σ_{int2} between the shells as well as the respective volumes of core and first shell:

$$V_c = \frac{4\pi}{3}\epsilon R_c^3 \tag{6}$$

$$V_{s1} = \frac{4\pi}{3}(R_c + d_1)^2(\epsilon R_c + d_1) - V_c \tag{7}$$

The second shell of hydrated polymer has a constant thickness d_2 and is modeled with a density profile $\propto r^{-4/3}$ according to the Halperin theory[43] for starlike micelles

https://dx.doi.org/10.1021/acs.macromol.0c01936
Macromolecules 2020, 53, 10686−10698

$$A_{s2}(Q,\alpha) = \frac{1}{C} e^{-Q^2 {\sigma_{int2}}^2/2} \times \int_{R_{s1,eff}}^{\infty} 4\pi r^2 \frac{r^{-4/3}}{1+\exp\frac{r-R_{s2,eff}}{\sigma_{out}R_{s2,eff}}} \frac{\sin Qr}{Qr} dr \quad (8)$$

A Fermi-like cutoff function at the effective micellar radius $R_{s2,eff} = R_{s1,eff} + d_2$ with width σ_{out} was introduced to account for the finite length of the polymer blocks and C is a normalization constant:

$$C = \int_{R_{s1,eff}}^{\infty} 4\pi r^2 \frac{r^{-4/3}}{1+\exp\frac{r-R_{s2,eff}}{\sigma_{out}R_{s2,eff}}} dr \quad (9)$$

The density profiles assumed in this model, including rough interfaces, are sketched in Figure 1c. Finally, the model considers the so-called "blob" scattering,[44] a scattering contribution arising from the internal polymer structure in the second shell:

$$B(Q) = \frac{P_{Beau}(Q)}{1+\nu P_{Beau}(Q)} \quad (10)$$

where ν is an effective surface coverage and $P_{Beau}(Q)$ is the Beaucage form factor.[45]

The actual fit parameters of the model are the aggregation number N_{agg}, the thicknesses d_1 and d_2 of the shells, the asphericity ϵ, the interface roughnesses σ_{int1} and σ_{int2}, the radius of gyration R_g in the Beaucage form factor, and the surface coverage ν. The relative width of the outer surface was fixed at $\sigma_{out} = 0.1$, based on previous studies.[15,19] All other model parameters are calculated in the following way: The molecular volume of an n-alkyl chain is calculated from its molecular weight and density, $V_{M,Cn} = M_{Cn}/d_{Cn}$, which determines the core radius via

$$N_{agg}V_{M,Cn} = \frac{4\pi}{3}\epsilon {R_c}^3 \quad (11)$$

The partial molecular volume of a single PEO chain in the dehydrated layer is $V_{M,PEO,s1} = V_{s1}/N_{agg}$ and therefore the mass fraction of PEO in the first shell

$$X_{s1} = \frac{d_{PEO,s1}V_{M,PEO,s1}}{M_{PEO}} \quad (12)$$

This leaves the remaining partial PEO molecular volume in the hydrated second shell to be

$$V_{M,PEO,s2} = (1-X_{s1})M_{PEO}/d_{PEO,s2} \quad (13)$$

so that the overall micellar volume becomes $V_{mic} = N_{agg}(V_{M,Cn} + V_{M,PEO,s1} + V_{M,PEO,s2})$. Lastly, the molecular volume of a solvent molecule is $V_{M,solv} = M_{solv}/d_{solv}$. With these quantities and the respective scattering lengths b_x, the scattering length densities are calculated as

$$\rho_c = b_{Cn}/V_{M,Cn} \quad (14a)$$

$$\rho_{s1} = X_{s1}b_{PEO}/V_{M,PEO,s1} \quad (14b)$$

$$\rho_{s2} = (1-X_{s1})b_{PEO}/V_{M,PEO,s2} \quad (14c)$$

$$\rho_{solv} = b_{solv}/V_{M,solv} \quad (14d)$$

and the contrasts are

$$\Delta\rho_{c/s1/s2} = \rho_{c/s1/s2} - \rho_{solv} \quad (15)$$

Finally, the scattering cross section of the micelle is[a]

$$\left(\frac{d\sigma}{d\Omega}\right)_{mic}(Q) = \int_0^{\pi/2} [{V_c}^2{\Delta\rho_c}^2{A_c}^2(Q,\alpha) + {V_{s1}}^2{\Delta\rho_{s1}}^2{A_{s1}}^2(Q,\alpha) + N_{agg}\left(N_{agg} - \frac{1}{1+\nu}\right) {V_{M,PEO,s2}}^2{\Delta\rho_{s2}}^2{A_{s2}}^2(Q,\alpha) + 2V_cV_{s1}\Delta\rho_c\Delta\rho_{s1}A_c(Q,\alpha)A_{s1}(Q,\alpha) + 2V_cN_{agg}V_{M,PEO,s2}\Delta\rho_c\Delta\rho_{s2}A_c(Q,\alpha)A_{s2}(Q,\alpha) + 2V_{s1}N_{agg}V_{M,PEO,s2}\Delta\rho_{s1}\Delta\rho_{s2}A_{s1}(Q,\alpha)A_{s2}(Q,\alpha)] \sin\alpha \, d\alpha \quad (16)$$

where the integration over α performs a rotational average to account for the anisotropic shape of the micelle. With the blob scattering added incoherently, the overall macroscopic scattering cross section then is

$$\frac{d\Sigma}{d\Omega}(Q) = \frac{\phi}{V_{mic}}\left[\left(\frac{d\sigma}{d\Omega}\right)_{mic}(Q) + N_{agg}{V_{M,PEO,s2}}^2{\Delta\rho_{s2}}^2B(Q)\right] \quad (17)$$

The scattering model was used to simultaneously analyze the SAXS and SANS data of C_{28}-dhPEO5.

RESULTS AND DISCUSSION

Core Crystallization in *n*-Alkyl-PEO Micelles. Previous SAXS experiments in combination with density measurements and differential scanning calorimetry (DSC) have shown the n-alkyl cores in C_n-PEOx micelles crystallize.[19,21,23,29] Increasing the temperature above the melting point T_m, melting of the n-alkyl chains can be observed in the SAXS curves by a significant increase in the core scattering contribution caused by the lowered n-alkyl density and therefore increased core contrast (see Figure 2a for an example data set of C_{28}-PEO5). In addition, DSC melting traces revealed a clear endothermic phase transition at T_m (see Figure 2b). By comparing the melting enthalpy obtained from DSC with the melting enthalpy of the corresponding bulk n-alkanes, we could estimate a degree of crystallinity around 30−50%.[19,28] Furthermore, our observed transition temperatures are quite close to the bulk melting temperatures of corresponding n-alkanes,[32] and the difference can be excellently described by a simple Gibbs−Thomson behavior.[23,29] Nonetheless, one cannot describe the state of the n-alkane blocks within the core as crystalline in a classical sense because the maximum domain size is very small as it is constrained by the micellar core radius R_c. To obtain direct evidence of the n-alkyl crystallization and information about their conformation inside the crystalline domains, we performed wide-angle X-ray scattering (WAXS) experiments on selected C_n-PEOx micelles. Because the crystallites inside the micellar cores are very small ($\leq R_c$), any Bragg peaks are heavily affected by Scherrer broadening.[46] Therefore, to increase the chances of observing Bragg scattering, we used a shorter PEO block, C_{28}-hPEO3, as this molecule forms larger micelles.[15] WAXS data above and below the melting point are shown in Figure 2c together with data from hPEO3 homopolymer in solution. As evidenced by the hPEO3 reference data, the main features of the C_{28}-hPEO3 WAXS curves originate from the hPEO3 corona. Only the large peak around $Q \approx 1-2$ Å^{-1} seems to stem from the n-alkyl

https://dx.doi.org/10.1021/acs.macromol.0c01936
Macromolecules 2020, 53, 10686−10698

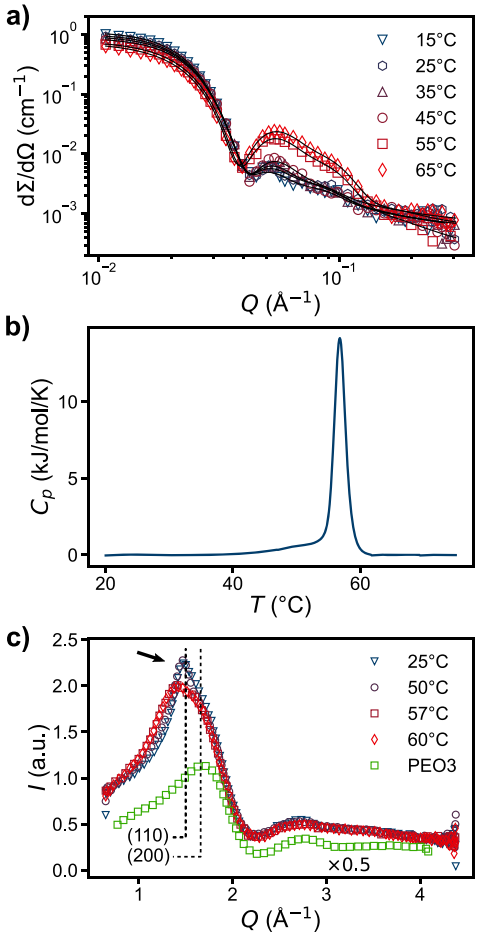

Figure 2. (a) Temperature-dependent SAXS curves of C_{28}-hPEO5 in H_2O, taken from ref 19. Note the increased core scattering contribution at intermediate Q for $T \geq 55$ °C. (b) NanoDSC trace of C_{28}-hPEO5 in H_2O, also taken from ref 19. The melting point is at $T_m \approx 57$ °C. (c) WAXS curves of C_{28}-hPEO3 at 5 vol % above and below the melting transition. The arrow marks a pronounced spike that vanishes below the melting transition. For comparison, the positions of the dominant (110) and (200) Bragg reflections of the normal *n*-alkane orthorhombic crystal lattice are indicated. In addition, a scaled WAXS curve of hPEO3 homopolymer is shown.

core. Interestingly, there is a pronounced spike on top of it (marked by an arrow) that vanishes above the melting transition. The exact same effect, only less pronounced, was also observed in C_{28}-hPEO5 micelles, shown in Figure S1. We identify this feature at Q = 1.5 Å^{-1} as the dominant (110) reflection of the normal *n*-alkane orthorhombic crystal lattice,[47] which was also found by Yin and Hillmyer[48] in crystalline polyethylene micellar cores as well as by Fu et al.[49] in *n*-alkanes confined in microcapsules. Both groups, however, also observed the second-most dominant (200) reflection at 1.66 Å^{-1}, but since it is much weaker than the (110) reflection, it is not discernible in our data. Nonetheless, we conclude that the crystalline *n*-alkyl chains in C_n-PEO*x* micellar cores adopt a conformation similar to that in bulk.

Effect of Crystallization on the Core Shape. In all our previous works on the C_n-PEO*x* system, we used a spherical core−shell model for starlike micelles which yielded very good agreement with experimental small-angle scattering data (see for instance Figure 2a).[15,16,19,20,23,29] However, it is not obvious how (partially) crystalline *n*-alkyl chains could be arranged in a spherical core. Vilgis and Halperin predicted that diblock copolymers with crystallizing solvophobic blocks would form disklike cores, where the core chains align along their axis and the solvophilic chains stick out from the basal planes.[50,51] These micelles are only stable in the starlike limit, though, when the corona chains are much longer than the core chains. Interestingly, in this case the corona would still be approximately spherical, rendering it hard to discriminate them from regular spherical starlike micelles unless the structure of the core can be isolated experimentally. Therefore, we set out to have a closer look on the actual core shape. Neutron scattering offers an opportunity to investigate the core selectively because of the unique dependence of the scattering signal on the isotopic composition of the sample. For this purpose, we prepared C_{28}-dhPEO5 with 82% deuterated PEO which has almost no contrast to D_2O, enhancing the scattering signal of the *n*-alkyl core.

The SANS data are shown in Figure 3a and were merged together from a low- and high-concentration sample as described in the Experimental Section (individual data sets shown in the Supporting Information). The temperature was increased stepwise from 40 to 70 °C to reveal changes during the melting transition. Indeed, there is a very distinct change in the scattering pattern between 55 and 57 °C. In addition, the same samples were measured with SAXS at 40 and 70 °C which serves as comparison with dominant corona scattering (see Figure 3b,c). These SAXS curves can be fitted very well with our established spherical core−shell model for starlike micelles, but we were not able to reproduce the core-selective SANS data with reasonable parameters. Therefore, we created a micellar scattering model with an anisotropic core shape but approximately spherical corona which was introduced in detail above. Although Halperin and Vilgis suggested a cylindrical or disklike shape for crystalline micellar cores,[50,51] we chose an ellipsoidal model. Considering that the hydrocarbon core is only partially crystalline and that the hydrophilic blocks have a disordering effect, we deemed a proper disklike shape unlikely. Furthermore, a globular shape reduces the unfavorable core−corona interface area. It also allows a flexible description of possible shapes, from more compressed, almost disklike, oblates to more elongated, prolate shapes. In any case, the scattering signals of cylindrical and ellipsoidal shapes are barely discernible, so that a distinction is without practical importance (compare Figure S2).

The ellipsoidal core−shell model did, though, still deviate systematically from the experimental data in the intermediate Q range, indicating that there was an additional scattering contribution from a structure on a length scale between core and shell. We finally were able to reproduce all scattering curves satisfactorily (black lines in Figure 3) by assuming a thin layer of dehydrated PEO just around the core, where the polymer volume fraction is highest. Such a layer can occur when the polymer grafting density on the core surface is very high.[52,53] As PEO is known to phase-separate at high concentrations,[54] it is particularly prone to form such a dehydrated layer, which has been reported for densely PEO-grafted nanoparticles.[55−57] These two new features, aspherical core and dehydrated PEO layer, have not been detected before because the starlike PEO corona dominates the scattering signal under usual full-contrast conditions. Also, since $d_1 + d_2 \gg R_c$, the overall micelle appears approximately spherical despite an ellipsoidal core (compare Figure 1b). The model fits still deviate from the SANS data at lowest Q. These data

https://dx.doi.org/10.1021/acs.macromol.0c01936
Macromolecules 2020, 53, 10686−10698

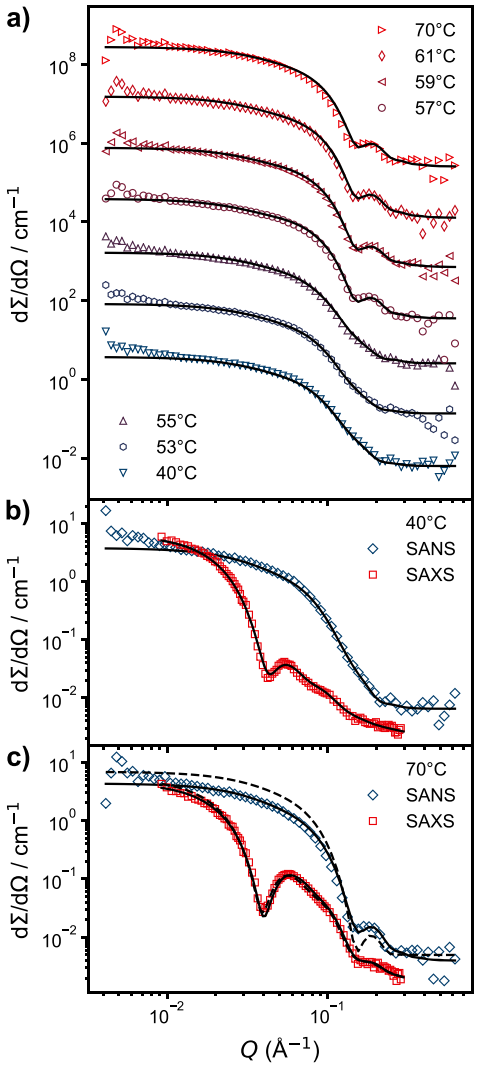

Figure 3. (a) SANS curves of C_{28}-dhPEO5 in D_2O at increasing temperatures around the melting transition. The data have been shifted by factors of 20 for the sake of clarity. Black lines represent model fits which are discussed in more detail in the main text. (b) Simultaneous fit of SAXS and SANS data at 40 °C. (c) Simultaneous fit of SAXS and SANS data at 70 °C. The black dashed line is a simultaneous fit using our conventional, spherical core−corona model.

points, though, have a high experimental uncertainty because of their sensitivity to exact subtraction of primary beam contributions and are thus considered less relevant. It should also be noted that a spherical core with dehydrated PEO layer does not agree with the SANS data; both ellipsoidal deformation and a dehydrated layer are necessary to obtain good agreement. On the other hand, we cannot exclude inhomogeneity in the thickness of the inner PEO layer, d_1. For instance, in areas of high core surface curvature, the polymer crowding is expected to be less severe, and thus the dehydration layer could be thinner. However, the resolution of SANS experiments is not good enough to resolve such minor details, and we therefore chose the simplest option, a constant layer thickness around the core.

The consistency of the new anisotropic model with our previous results using a spherical core−shell model was ensured by fitting SAXS and SANS data simultaneously at 40 and 70 °C. The main fitting parameters are shown in Table 2, whereas an extensive listing of all parameters is given in Table S1. Fit parameters were the aggregation number N_{agg}, the thicknesses d_1 and d_2 of the shells, the asphericity ϵ, the interface roughnesses σ_{int1} and σ_{int2}, the radius of gyration R_g in the Beaucage form factor, and the surface coverage ν. The scattering lengths b_x were calculated based on the polymer characterization (Table 1) and tabulated atomic scattering lengths.[58] To simplify calculations and facilitate comparison with literature data, PEO parameters other than b_{PEO} were calculated as if the polymer was fully proteated. The densities of the C_{28} core and hydrated PEO shell are based on previous results,[19] and the density of the dehydrated PEO shell was assumed to equal the bulk PEO density.[59] Densities needed to be slightly adjusted to fit the SAXS data (see Table S1). The temperature-dependent density of D_2O was taken from ref 60. Because the contrast of the hydrated PEO is very low in the SANS experiments (compare Table S1), the latter are insensitive to R_g and ν and also d_2 and σ_{int2} are rather ill-defined. The overall micellar radius $R_m = R_c + d_1 + d_2 \approx 105-120$ Å as well as the $R_g \approx 50$ Å, determined mostly from the SAXS data, though, are in perfect agreement with previous findings.[19] Also, the temperature-independent N_{agg} has been reported in the same article. Furthermore, the interface roughness between the *n*-alkyl core and the dehydrated PEO shell decreases slightly above the melting transition. Supposedly, the partially crystalline C_{28} chains are incommensurate with a smooth interface while the molten state allows a more effective packing. In the crystalline phase, the core diameter along the short axis is about $2\epsilon R_c \approx 36$ Å. Tanford[4] calculated the length of a fully stretched *n*-alkyl tail as $l \approx (1.5 + 1.265(n-1))$ Å, which for C_{28} gives about 36 Å. Therefore, at least in the middle of the ellipsoidal core, the C_{28} chains can adopt an all-trans conformation, while the spatial

Table 2. Main Model Parameters Used for the Fits Shown in Figure 3[a]

	N_{agg}	d_1 (Å)	d_2 (Å)	ϵ	σ_{int1} (Å)	σ_{int2} (Å)	R_c[c] (Å)
SAXS 40 °C	140 ± 10	6 ± 2	76 ± 5	0.48 ± 0.05	4.3 ± 1.2	10.8 ± 4.0	37
SANS 40 °C	*b*	*b*	*b*	*b*	*b*	*b*	*b*
SANS 53 °C	131 ± 15	10 ± 4	75 ± 25	0.50 ± 0.05	4.0 ± 2.0	7.0 ± 7.0	36
SANS 55 °C	125 ± 10	12 ± 5	85 ± 25	0.51 ± 0.05	3.5 ± 1.0	9.2 ± 5.0	36
SANS 57 °C	135 ± 10	7 ± 3	90 ± 25	0.73 ± 0.05	2.5 ± 1.0	5.0 ± 5.0	33
SANS 59 °C	130 ± 10	9 ± 5	80 ± 25	0.72 ± 0.04	2.0 ± 1.0	5.0 ± 5.0	33
SANS 61 °C	135 ± 10	6 ± 3	75 ± 25	0.72 ± 0.04	2.0 ± 1.0	5.0 ± 4.0	33
SAXS 70 °C	130 ± 10	7 ± 2	67 ± 5	0.72 ± 0.05	2.0 ± 1.0	9.0 ± 4.0	33
SANS 70 °C	*b*	*b*	*b*	*b*	*b*	*b*	*b*

[a]The complete set is given in Table S1. [b]SANS and SAXS fitted simultaneously. [c]Calculated via eq 11.

https://dx.doi.org/10.1021/acs.macromol.0c01936
Macromolecules 2020, 53, 10686−10698

constraints toward the rim may lead to some molecular disorder.

The most striking finding, however, is that the asphericity ϵ changes abruptly from ∼0.5 to ∼0.7 at the melting transition (T_m = 57 °C), which causes the very distinct change in the shape of the scattering curves in Figure 3a. The evolution of ϵ is also plotted in Figure 4b. This means the micellar core is a

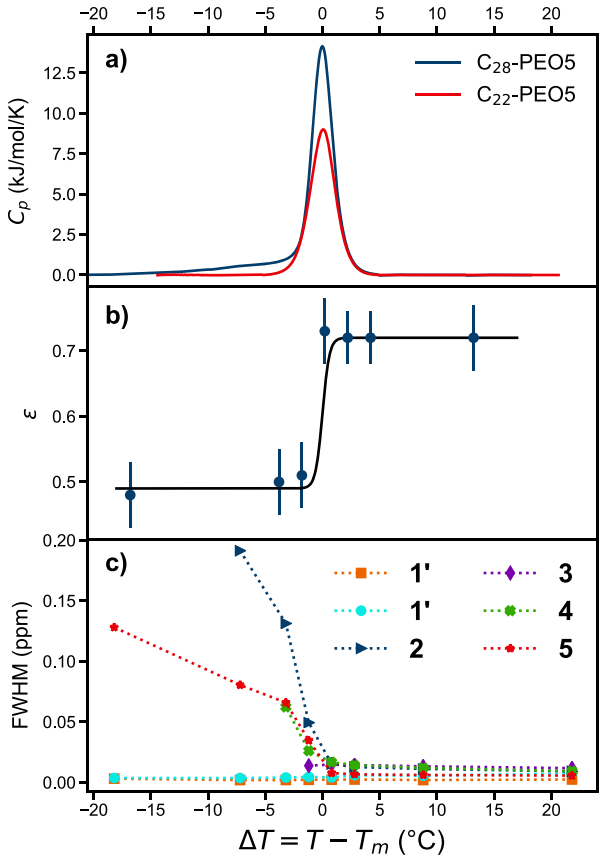

Figure 4. (a) Melting curves of C_{28}- and C_{22}-hPEO5 determined by Nano DSC, taken from ref 19. (b) Asphericity ϵ of the C_{28}-dhPEO5 micellar core, determined from the fits in Figure 3a. The black line is a guide to the eye. (c) FWHM of the characteristic C_{22}-dPEO5 ^{1}H NMR signals as assigned in Figure 5.

rather flat oblate ellipsoid below the melting transition,[b] almost disklike as proposed by Halperin and Vilgis, since *n*-alkyl chains crystallize parallel to each other. Somehow surprisingly, though, the core does not become completely spherical above the melting transition, either, but instead maintains a somewhat oblate shape, as can be seen from $\epsilon < 1$. The effect might be explained by the fact that the uniform *n*-alkyl chains still preferably align in parallel, but the driving force for alignment is weaker above the melting temperature. The Kuhn length of poly(ethylene), in principle a very long linear alkane, is ∼14 Å,[61] corresponding to about 11 CH_2 repeat units. Thus, the C_{28} alkyl block has on average only 1−2 kinks in the liquid state, which means that it is still rather rigid, explaining the persisting core anisotropy. This explanation is supported by computer simulations of Lin et al., who found a gradual transition from disk to sphere with decreasing core block rigidity.[62] Furthermore, Vuorte et al. simulated C_{18}-PEO micelles with noncrystalline cores. They also found a slight anisotropy which might become more pronounced with longer *n*-alkyl chains.[18] In addition, the persistent core anisotropy in the liquidlike phase can be explained by dynamic fluctuations of the core. As these fluctuations occur on time scales much shorter than the temporal resolution of the scattering experiment, only an averaged ellipsoidal shape is observable. Applying polydispersity in the asphericity ϵ would unnecessarily complicate the scattering model, though, and is therefore omitted here.

Even though to our knowledge the data set presented here is the most extensive experimental study of core shape change around the melting transition, similar disk−sphere transitions have been reported in the literature.[48,63−67] For example, Yin and Hillmyer compared poly(*N*,*N*-dimethylacrylamide)−polyethylene (PDMA−PE) and poly(*N*,*N*-dimethylacrylamide)−poly(ethylene-*alt*-propylene) (PDMA−PEP) in water with TEM and SANS.[48,65] At 120 °C, both polymers formed spherical micelles with a PDMA corona surrounding the hydrophobic core. When cooled to room temperature, however, the PE block crystallized and forced the core into an oblate ellipsoidal shape while the PEP core remained amorphous and spherical. We would like to highlight that the PDMA−PE system is kinetically frozen so there is no molecular exchange between micelles and the system cannot attain the thermodynamically most favorable state.[48] In contrast, C_{28}-dhPEO5 exhibits active chain exchange, and even at the lowest experimental temperature, 40 °C, molecular exchange takes place within minutes.[23] Interestingly, the aggregation number still remains unchanged above the melting temperature, and only the core shape is altered.

However, crystallization does not always imply an anisotropic core shape. For instance, the simulations of oligo(ethylene sulfide)−poly(ethylene glycol) (OES−PEG) by Sevgen et al. revealed a spherical core shape, even though the OES chains partially crystallized.[68] In other cases, crystallization leads to aggregation into micellar worms[65,69−71], which is often exploited in CDSA, or it even leads to precipitation.[72] Thus, the effect of core crystallization on the micellar shape cannot be universally predicted but instead depends strongly on the individual polymer architecture.

The other new feature of C_n-PEO*x* micelles, which has been found in this study, is the existence of a thin layer of dehydrated PEO around the C_{28} core (compare d_1 in Table 2). In previous works,[19,29] we investigated the melting point depression in the nanometer-sized micellar *n*-alkyl cores compared to bulk *n*-alkanes by means of a generalized Gibbs−Thomson equation.[73] The analyses revealed an unusually low interfacial tension between core and corona, around 8−9 mN/m,[19,29] while the *n*-alkane/water interfacial tension is typically around 50−60 mN/m.[12,74,75] Apparently, the dehydrated PEO layer shields the *n*-alkyl chains from the solvent. The interfacial tension between PEO and alkanes is around 9−12 mN/m,[76,77] which coincides much better with the interfacial tension between core and corona we found in the Gibbs−Thomson analysis. The dehydrated PEO layer has not been discovered before because the densities of melt and solution PEO are not very different (compare Table S1), and the hydrated PEO corona has a much greater volume compared to the dehydrated shell. Only when the outer corona is nearly matched out, as in this study, the contrast conditions are shifted so that the inner layer becomes visible. Apparently, PEO dehydrates in the immediate vicinity of the core simply because of spatial constraints, imposed by the

https://dx.doi.org/10.1021/acs.macromol.0c01936
Macromolecules 2020, 53, 10686−10698

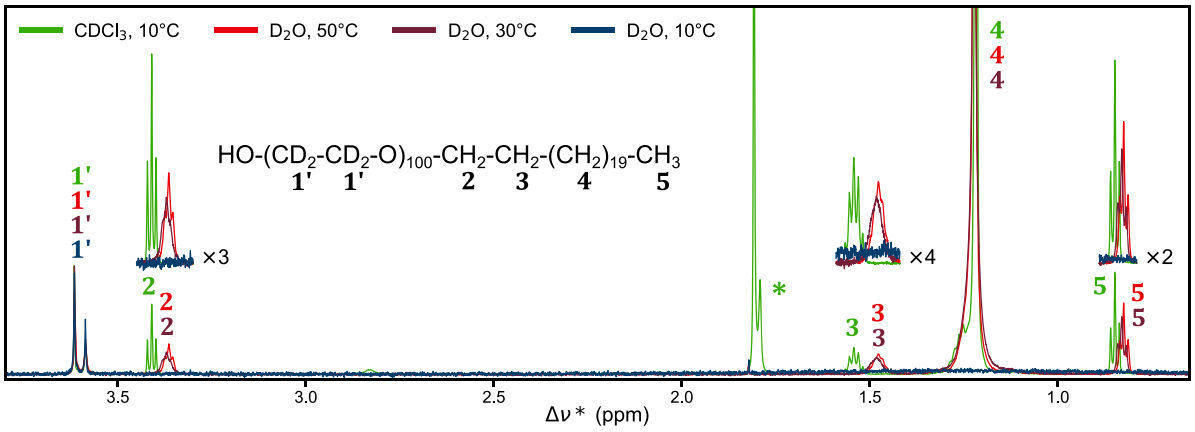

Figure 5. ^{1}H NMR spectra of C_{22}-dPEO in $CDCl_3$ and D_2O. The D_2O spectra were shifted and scaled so that the residual hPEO signals (**1′**) overlap with the $CDCl_3$ spectrum. ∗ originates from residual H_2O.

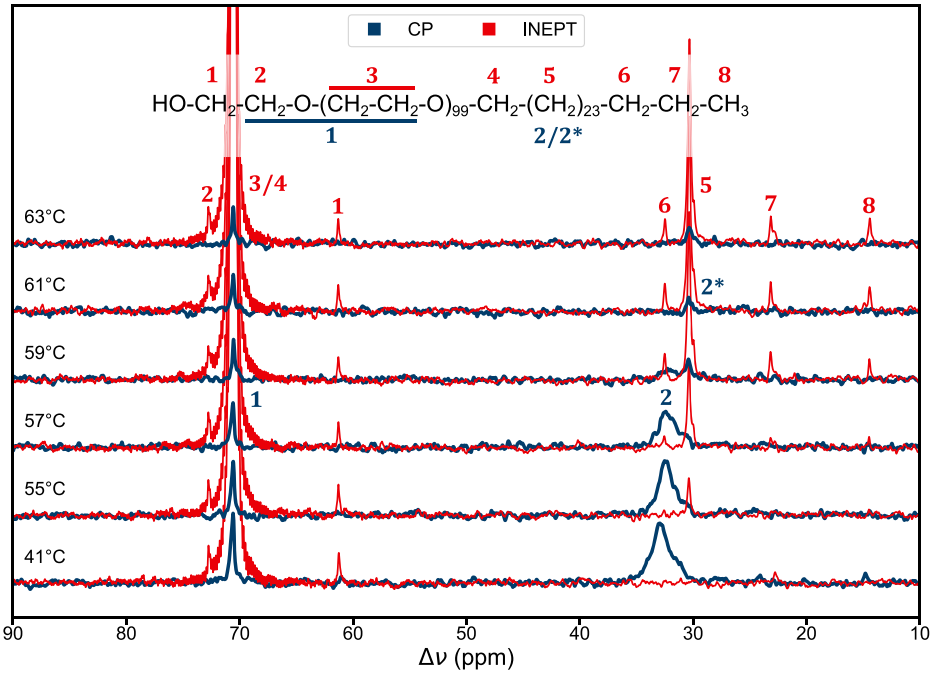

Figure 6. CP and INEPT ^{13}C ssNMR spectra of a C_{28}-hPEO gel in D_2O. A clear phase transition is visible around T_m = 57 °C.

rather high grafting density of ∼1.1 nm^{-2}. The phenomenon has been experimentally found on densely polymer-grafted nanoparticles[55,56] by using SAS. Maccarini et al. observed an ∼17 Å dehydrated PEO layer on gold nanoparticles with a grafting density of almost 6 nm^{-2}, and Grünewald et al. reported an ∼25 Å dehydrated PEO layer on iron oxide nanoparticles with a grafting density of 3.5 nm^{-2}. Recently, Dahal et al. employed computer simulations to investigate the phenomenon more systematically.[57] They simulated gold nanoparticles of various sizes and PEO grafting densities and found a distinct dehydration layer of up to 15 Å when the grafting density was higher than 1.5 nm^{-2}. However, also for lower grafting densities, they observed a thin dehydration layer of ∼5 Å, which coincides with our findings. In our case, the dehydration of PEO might furthermore be promoted by the presence of alkyl blocks in the interfacial area.

***n*-Alkyl Block Conformation.** To further shed light on the conformation of the *n*-alkyl blocks inside the micellar core, we employed nuclear magnetic resonance (NMR) spectroscopy. First, we performed conventional ^{1}H solution NMR of C_{22}-dPEO micelles in D_2O to observe the change of the characteristic *n*-alkyl peaks with temperature and compared it to reference spectra in $CDCl_3$, a common solvent for both blocks where no micelles form. Example data including peak assignment are shown in Figure 5. In aqueous solution above the melting point (T_m = 29 °C), i.e., in the micellized state with liquidlike core, the *n*-alkyl peaks (**2**−**5** as assigned in Figure 5) are slightly broadened compared to the unimeric state in deuterochloroform, indicating a minor reduction in mobility due to micellization. This agrees with the findings of Ortony et al., who investigated the internal dynamics of an *n*-alkyl-functionalized, self-assembling peptide using electron paramagnetic resonance spectroscopy[78] and found the alkyl blocks buried in the fiber core to have a reduced rotational diffusion rate compared to fully liquid *n*-alkanes in the melt. When the temperature of the C_{22}-dPEO sample is reduced below the melting point, though, the NMR peaks become undetectably broad (compare the blue spectrum in Figure 5),

https://dx.doi.org/10.1021/acs.macromol.0c01936
Macromolecules 2020, 53, 10686−10698

which means that the *n*-alkyl chain mobility is strongly restricted. To investigate the peak broadening more quantitatively, we fitted the individual signals with Lorentzian curves, and the determined peak widths (full width at half-maximum, FWHM) are shown in Figure 4c while the fits are shown in Figure S3, together with a more detailed description of the fit procedure.

The width of the two residual hPEO peaks (**1′** as assigned in Figure 5) is unaltered over the entire temperature range while the *n*-alkyl peaks (**2**–**5**) are broadened very quickly below the melting point (compare Figures 4c and Figure S3). Interestingly, the inner carbons (**3** and **4**) are broadened immediately below the melting transition: Already at 25 °C they cannot be distinguished from the background anymore, whereas the PEO grafting site (**2**) and the terminal methyl group (**5**) can be distinguished at least down to 21 °C (compare Figure S3). This can be rationalized by the fact that the CH_2 group next to the PEO block is most effected by the free polymer and methyl groups generally are rather mobile, while the inner methylenes are more prone to order, which has also been revealed in the computer simulations of Sevgen et al.[68]

To investigate the internal dynamics of the *n*-alkyl blocks further, we employed magic-angle-spinning ^{13}C solid-state NMR spectroscopy (ssNMR). To this end, we produced a high-concentration C_{28}-hPEO gel in D_2O. First, we conducted INEPT and CP experiments at various temperatures around the melting transition, where CP signals arise from restricted, solidlike phases and INEPT signals originate from liquidlike CH bonds with a fast, isotropic reorientation.[79] The spectra are shown in Figure 6, and there is a clear phase transition around T_m = 57 °C. The peaks were assigned based on the results of Ferreira et al.,[80] who investigated a similar C_{12}-oligo(ethylene oxide) system. The most dominant peak, at 70 ppm, is the main PEO signal (**3**), and the resonance at 61 ppm stems from the terminal PEO carbon next to the OH group (**1**). The PEO block is clearly liquidlike, but there is also a CP signal at 70 ppm (**1**) which probably originates from the dehydrated PEO in the immediate vicinity of the core which undergoes anisotropic reorientation on account of being anchored to the core surface. The peaks at 24 and 14 ppm are the ultimate CH_2 (**5**) and terminal CH_3 group (**6**), respectively. They show a clear liquidlike behavior above the melting transition, but below the melting point the absence of INEPT peaks shows that the reorientational correlation time τ_c is longer than 10 ns.[81] Yet, no significant CP signal arises, which is in agreement with our conclusion from the ^1H NMR spectra that the terminal methyl group and the PEO grafting site remain relatively mobile below the melting transition ($\tau_c \approx$ 1–10 μs[81]). Furthermore, there is a strong signal at 31 ppm from the liquid *n*-alkyl chain above the melting point (**5**) which interestingly also exhibits a weak CP signal (**2***). This points toward a certain degree of anisotropy in the system which agrees with the aspherical core shape found in the SANS experiments. Finally, there is also an INEPT signal at 33 ppm from the penultimate CH_2 group (**6**) in the C_{28} chain. Below the melting point, there is a strong CP signal at the same chemical shift (**2**) which is characteristic for *n*-alkyl chains in the all-trans conformation.[82] The increased width of that signal indicates irregular packing, which is reasonable given the spatial constraints within the micellar core.

However, we wanted to further characterize the state of the hydrocarbon chains in the solid phase and therefore conducted CP $R_{1\rho}$ and R_1 experiments below the melting point. To determine the *n*-alkyl ^{13}C relaxation rate in the rotating frame $R_{1\rho}$, the integrated intensity of the CP peak **2** was measured as a function of the delay time t at different spin lock pulse nutation frequencies ν_1. These data were fitted with a relaxation function $I(t) = I_0 \exp(-R_{1\rho}t)$, shown in Figures S4–S6. In the same way, the relaxation rate in the laboratory frame, R_1, was obtained. This is shown in Figures S7–S9, and all resulting relaxation rates are plotted together in Figure 7.

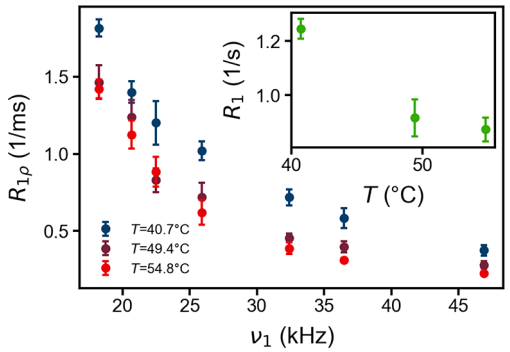

Figure 7. ^{13}C relaxation rate of all-trans *n*-alkyl blocks (**2** in Figure 6) in the rotating frame $R_{1\rho}$ and in the laboratory frame R_1 as a function of temperature and spin lock pulse nutation frequency ν_1.

The huge difference between $R_{1\rho}$ and R_1 indicates CH bond reorientation on the time scale of microseconds.[83] It should be noted, though, that the R_1 relaxation rates agree fairly well with values reported for C_{21}-PEO10-C_{21} hydrogels.[28] In summary, these results point toward a rotator-like phase with mostly all-trans conformation of the C_{28} blocks. Nonetheless, the molecular packing is perturbed due to the strong spatial confinement in the micellar core, and the bond reorientation is unusually slow, on the milli- to microseconds scale.

Finally, we performed INEPT-RPDLF experiments to analyze the anisotropy in the micellar core still present above the melting transition by calculating the orientational order parameter S_{CH}. To this end, we measured the integrated intensity of the INEPT signals (**3**, **5**–**8** in Figure 6) as a function of the delay time t_1, shown in Figure S10. For the strongest signal at 31 ppm (**5**), there is a clear minimum at $t_{1,min} \approx 16 \pm 1$ ms, which corresponds to a frequency splitting of $\Delta\nu_{CH} = \frac{2}{t_{1,min}} \approx 125 \pm 8$ Hz. With an effective scaling factor 0.315[84] this gives a dipolar coupling $d_{CH} = \Delta\nu_{CH}/0.315 \approx 400 \pm 25$ Hz. Estimating the maximum splitting for a static CH bond to be ~21 kHz,[85] we obtain an order parameter of $S_{CH} \approx$ 0.02, which agrees with the small but detectable CP signal **2***. At 57 °C, directly at the melting point, the minimum is slightly shifted to shorter delay times which indicates an increased S_{CH}. This seems reasonable given the system is on the brink of the solid phase. Even though the other alkyl signals **6**–**8** exhibit a much lower signal-to-noise ratio, they all follow the same trend. Albeit small, the orientational order parameter in the C_{28} block is finite and thus suggests some molecular order and/or asymmetry in the micellar core above the melting point, in agreement with the residual asphericity found in the SANS experiments. The absolute value of S_{CH} also agrees fairly with the work of Ferreira et al. on penta(ethylene glycol) mono-*n*-dodecyl ether (i.e., C_{12}-PEO0.25) lamellae in D_2O.[80]

https://dx.doi.org/10.1021/acs.macromol.0c01936
Macromolecules 2020, 53, 10686–10698

CONCLUSION AND OUTLOOK

In summary, we performed an extensive study of the nature of the *n*-alkyl core in partially crystalline C_n-PEO*x* micelles, both below and above the melting transition. Employing SANS and SAXS, we found the core to be elliptical below the melting transition, in agreement with theoretical predictions and other experimental findings. In addition, we observed a less pronounced but still significantly aspherical core above the melting point and relate this to the relative rigidity of the *n*-alkyl block, even in the liquidlike state, as well as thermal shape fluctuations. In fact, reports on related C_n-EO_m surfactant micelles with aspherical shape are numerous.[86−88] In the future, we aim to investigate the core shape of shorter *n*-alkyl blocks to see whether the asphericity persists. We furthermore reported a thin layer of dehydrated PEO in the immediate vicinity of the hydrocarbon core. To our knowledge, such a phenomenon has so far only been reported for metallic nanoparticles with extremely high grafting densities, but here we also observe it in polymeric micelles with moderate grafting density. In addition, we characterized the *n*-alkyl core using NMR. Above the melting transition, the core blocks are liquidlike, with low but finite orientational order in agreement with the persistent asphericity of the core. But below the melting transition, the system exhibits unusually high relaxation rates which point toward a rotator-like phase with mostly all-trans chain conformation and milli- to microseconds reorientation. This is further supported by the WAXS results where we observe a Bragg signal equivalent to normal *n*-alkane crystalline phases with orthorhombic chain packing. As C_n-PEO*x* is an excellent model for core-crystalline micelles which have attracted significant attention recently, our findings have implications for a wider field of ongoing research. We hope that this work inspires similar studies on other relevant systems with partially ordered cores.

ASSOCIATED CONTENT

Supporting Information

The Supporting Information is available free of charge at https://pubs.acs.org/doi/10.1021/acs.macromol.0c01936.

Detailed parameters of the ^{13}C ssNMR experiments; additional WAXS data; a complete listing of the SAS fit parameters; unmerged SANS data of low- and high-concentration C_{28}-dhPEO sample; comparison between the scattering patterns of ellipsoidal and cylindric shapes; details of the ^{1}H NMR line width analysis; additional plots for the determination of $R_{1\rho}$ and R_1; additional data for the determination of S_{CH} (PDF)

AUTHOR INFORMATION

Corresponding Authors

Lutz Willner − *Jülich Centre for Neutron Science (JCNS-1) and Institute of Biological Information Processing (IBI-8), Forschungszentrum Jülich GmbH, 52425 Jülich, Germany*; Email: l.willner@fz-juelich.de

Reidar Lund − *Department of Chemistry, University of Oslo, 0315 Oslo, Norway*; orcid.org/0000-0001-8017-6396; Email: reidar.lund@kjemi.uio.no

Authors

Nico König − *Department of Chemistry, University of Oslo, 0315 Oslo, Norway; Jülich Centre for Neutron Science (JCNS-1) and Institute of Biological Information Processing (IBI-8), Forschungszentrum Jülich GmbH, 52425 Jülich, Germany*

Göran Carlström − *Centre for Analysis and Synthesis, Department of Chemistry, Lund University, 22100 Lund, Sweden*; orcid.org/0000-0003-4981-2440

Thomas Zinn − *ESRF - The European Synchrotron, 38043 Grenoble, France*

Kenneth D. Knudsen − *Department for Neutron Materials Characterization, Institute for Energy Technology, 2027 Kjeller, Norway*

Frode Rise − *Department of Chemistry, University of Oslo, 0315 Oslo, Norway*

Daniel Topgaard − *Division of Physical Chemistry, Department of Chemistry, Lund University, Lund, Sweden*

Complete contact information is available at: https://pubs.acs.org/10.1021/acs.macromol.0c01936

Notes

The authors declare no competing financial interest.

ACKNOWLEDGMENTS

This work was partly supported by the Research Council of Norway through the Norwegian NMR Package in 1994 and the Norwegian NMR Platform, NNP (226244/F50), and also partly supported by the Department of Chemistry and the Faculty of Mathematics and Natural Sciences at University of Oslo. We have also received funding from the European Union's Horizon 2020 research and innovation program under grant agreement No. 731019 (EUSMI). Furthermore, we thank Najet Mahmoudi for great technical support during the SANS experiment at Sans2d.[35] Provision of X-ray beamtime by the Norwegian Centre for X-ray Diffraction, Scattering and Imaging (RECX) as well as the European Synchrotron Radiation Facility (ESRF, France) is also acknowledged. Finally, we thank the Institute for Energy Technology (IFE, Norway) and Heinz Maier-Leibnitz Zentrum (MLZ, Germany) for giving access to do preliminary SANS experiments.

ADDITIONAL NOTES

[a]The correction factor $1 = 1 + \nu$ in the outer shell scattering results from the blob scattering.

[b]Even though the characteristic scattering curves of oblate and prolate ellipsoids are relatively similar, we could distinguish between the two shapes based on the high-*Q* data provided by the high-concentration sample.

REFERENCES

(1) Alexandridis, P.; Lindman, B. *Amphiphilic Block Copolymers: Self-Assembly and Applications*; Elsevier: 2000.

(2) Hamley, I. W. *Block Copolymers in Solution: Fundamentals and Applications*; John Wiley & Sons: 2005.

(3) Tritschler, U.; Pearce, S.; Gwyther, J.; Whittell, G. R.; Manners, I. 50th Anniversary Perspective: Functional Nanoparticles from the Solution Self-Assembly of Block Copolymers. *Macromolecules* **2017**, *50*, 3439−3463.

(4) Tanford, C. *The Hydrophobic Effect: Formation of Micelles and Biological Membranes*, 2nd ed.; Krieger: Malabar, FL, 1991; p ix, 233 pp.

(5) Voets, I. K.; de Keizer, A.; Cohen Stuart, M. A. Complex coacervate core micelles. *Adv. Colloid Interface Sci.* **2009**, *147−148*, 300−318.

(6) Crassous, J. J.; Schurtenberger, P.; Ballauff, M.; Mihut, A. M. Design of block copolymer micelles via crystallization. *Polymer* **2015**, *62*, A1−A13.

(7) Jin, X. H.; Price, M. B.; Finnegan, J. R.; Boott, C. E.; Richter, J. M.; Rao, A.; Menke, M.; Friend, R. H.; Whittell, G. R.; Manners, I. Long-range exciton transport in conjugated polymer nanofibers prepared by seeded growth. *Science* **2018**, *360*, 897−900.
(8) Coe, Z.; Weems, A.; Dove, A. P.; O'Reilly, R. K. Synthesis of Monodisperse Cylindrical Nanoparticles via Crystallization-driven Self-assembly of Biodegradable Block Copolymers. *J. Visualized Exp.* **2019**, DOI: 10.3791/59772.
(9) Foster, J. C.; Varlas, S.; Couturaud, B.; Coe, Z.; O'Reilly, R. K. Getting into Shape: Reflections on a New Generation of Cylindrical Nanostructures' Self-Assembly Using Polymer Building Blocks. *J. Am. Chem. Soc.* **2019**, *141*, 2742−2753.
(10) Ganda, S.; Stenzel, M. H. Concepts, fabrication methods and applications of living crystallization-driven self-assembly of block copolymers. *Prog. Polym. Sci.* **2020**, *101*, 101195.
(11) Lodish, H.; Berk, A.; Zipursky, S. L.; Matsudaira, P.; Baltimore, D.; Darnel, J. *Molecular Cell Biology*; W. H. Freeman: New York, 2000.
(12) Ameri, M.; Attwood, D.; Collett, J. H.; Booth, C. Self-assembly of alcohol ethoxylate non-ionic surfactants in aqueous solution. *J. Chem. Soc., Faraday Trans.* **1997**, *93*, 2545−2551.
(13) Lafleche, F.; Nicolai, T.; Durand, D.; Gnanou, Y.; Taton, D. Association of Adhesive Spheres Formed by Hydrophobically End-Capped PEO. 2. Influence of the Alkyl End-Group Length and the Chain Backbone Architecture. *Macromolecules* **2003**, *36*, 1341−1348.
(14) Sommer, C.; Pedersen, J. S.; Garamus, V. M. Structure and Interactions of Block Copolymer Micelles of Brij 700 Studied by Combining Small-Angle X-ray and Neutron Scattering. *Langmuir* **2005**, *21*, 2137−2149.
(15) Zinn, T.; Willner, L.; Lund, R.; Pipich, V.; Appavou, M. S.; Richter, D. Surfactant or block copolymer micelles? Structural properties of a series of well-defined n-alkyl-PEO micelles in water studied by SANS. *Soft Matter* **2014**, *10*, 5212−20.
(16) Amann, M.; Willner, L.; Stellbrink, J.; Radulescu, A.; Richter, D. Studying the concentration dependence of the aggregation number of a micellar model system by SANS. *Soft Matter* **2015**, *11*, 4208−17.
(17) Zinn, T.; Willner, L.; Knudsen, K. D.; Lund, R. Self-Assembly of Mixtures of Telechelic and Monofunctional Amphiphilic Polymers in Water: From Clusters to Flowerlike Micelles. *Macromolecules* **2017**, *50*, 7321−7332.
(18) Vuorte, M.; Määttä, J.; Sammalkorpi, M. Simulations Study of Single-Component and Mixed n-Alkyl-PEG Micelles. *J. Phys. Chem. B* **2018**, *122*, 4851.
(19) König, N.; Willner, L.; Lund, R. Structure and thermodynamics of mixed polymeric micelles with crystalline cores: tuning properties via co-assembly. *Soft Matter* **2019**, *15*, 7777−7786.
(20) Zinn, T.; Willner, L.; Lund, R.; Pipich, V.; Richter, D. Equilibrium exchange kinetics in n-alkyl−PEO polymeric micelles: single exponential relaxation and chain length dependence. *Soft Matter* **2012**, *8*, 623−626.
(21) Zinn, T.; Willner, L.; Pipich, V.; Richter, D.; Lund, R. Effect of Core Crystallization and Conformational Entropy on the Molecular Exchange Kinetics of Polymeric Micelles. *ACS Macro Lett.* **2015**, *4*, 651−655.
(22) Zinn, T.; Willner, L.; Pipich, V.; Richter, D.; Lund, R. Molecular Exchange Kinetics of Micelles: Corona Chain Length Dependence. *ACS Macro Lett.* **2016**, *5*, 884−888.
(23) König, N.; Willner, L.; Pipich, V.; Zinn, T.; Lund, R. Cooperativity during Melting and Molecular Exchange in Micelles with Crystalline Cores. *Phys. Rev. Lett.* **2019**, *122*, 078001.
(24) König, N.; Willner, L.; Pipich, V.; Mahmoudi, N.; Lund, R. Tale of Two Tails: Molecular Exchange Kinetics of Telechelic Polymer Micelles. *Phys. Rev. Lett.* **2020**, *124*, 197801−1−6.
(25) Renou, F.; Nicolai, T.; Nicol, E.; Benyahia, L. Structure and Viscoelasticity of Mixed Micelles Formed by Poly(ethylene oxide) End Capped with Alkyl Groups of Different Length. *Langmuir* **2009**, *25*, 515−521.
(26) Zinn, T.; Willner, L.; Lund, R. Telechelic Polymer Hydrogels: Relation between the Microscopic Dynamics and Macroscopic Viscoelastic Response. *ACS Macro Lett.* **2016**, *5*, 1353−1356.
(27) Heatley, F.; Teo, H. H.; Booth, C. Proton longitudinal and transverse magnetic relaxation in dilute aqueous solutions of poly(oxyethylene) alkyl ethers. *J. Chem. Soc., Faraday Trans. 1* **1984**, *80*, 981−991.
(28) Knowles, P. R.; Barlow, R. J.; Heatley, F.; Booth, C.; Price, C. A study of chain dynamics in water-swollen gels of poly(ethylene oxide) dialkyl ethers using NMR and differential scanning calorimetry. *Macromol. Chem. Phys.* **1994**, *195*, 2547−2558.
(29) Zinn, T.; Willner, L.; Lund, R. Nanoscopic confinement through self-assembly: crystallization within micellar cores exhibits simple Gibbs-Thomson behavior. *Phys. Rev. Lett.* **2014**, *113*, 238305.
(30) Plazzotta, B.; Dai, J.; Behrens, M. A.; Furó, I.; Pedersen, J. S. Core Freezing and Size Segregation in Surfactant Core−Shell Micelles. *J. Phys. Chem. B* **2015**, *119*, 10798−10806.
(31) Dai, J.; Alaei, Z.; Plazzotta, B.; Pedersen, J. S.; Furó, I. Release of Solubilizate from Micelle upon Core Freezing. *J. Phys. Chem. B* **2017**, *121*, 10353−10363.
(32) Dirand, M.; Bouroukba, M.; Chevallier, V.; Petitjean, D.; Behar, E.; Ruffier-Meray, V. Normal Alkanes, Multialkane Synthetic Model Mixtures, and Real Petroleum Waxes: Crystallographic Structures, Thermodynami Properties, and Crystallization. *J. Chem. Eng. Data* **2002**, *47*, 115−143.
(33) Amann, M. Micellar Structure, Interactions and Phase Behavior of C28-PEO Polymer Micelles Studied by HR-SANS. PhD Thesis, Westfälische Wilhelms-Universität Münster, 2017.
(34) Heenan, R. K.; Rogers, S. E.; Turner, D.; Terry, A. E.; Treadgold, J.; King, S. M. Small Angle Neutron Scattering Using Sans2d. *Neutron News* **2011**, *22*, 19−21.
(35) Krengel, U.; Sørensen, H.; Mahmoudi, N.; Lund, R.; König, N. *Small-Angle Neutron Scattering Studies of a Bacterial Colonization Factor*; STFC ISIS Neutron and Muon Source, 2019. .
(36) Hwang, T.; Shaka, A. Water Suppression That Works. Excitation Sculpting Using Arbitrary Wave-Forms and Pulsed-Field Gradients. *J. Magn. Reson., Ser. A* **1995**, *112*, 275−279.
(37) Hartmann, S. R.; Hahn, E. L. Nuclear Double Resonance in the Rotating Frame. *Phys. Rev.* **1962**, *128*, 2042−2053.
(38) Morris, G. A. Sensitivity enhancement in nitrogen-15 NMR: polarization transfer using the INEPT pulse sequence. *J. Am. Chem. Soc.* **1980**, *102*, 428−429.
(39) Thomas, D. M.; Bendall, M. R.; Pegg, D. T.; Doddrell, D. M.; Field, J. Two-dimensional 13C-1H polarization transfer J spectroscopy. *J. Magn. Reson. (1969-1992)* **1981**, *42*, 298−306.
(40) Torchia, D. A. The measurement of proton-enhanced carbon-13 T1 values by a method which suppresses artifacts. *J. Magn. Reson. (1969-1992)* **1978**, *30*, 613−616.
(41) Dvinskikh, S. V.; Zimmermann, H.; Maliniak, A.; Sandström, D. Measurements of motionally averaged heteronuclear dipolar couplings in MAS NMR using R-type recoupling. *J. Magn. Reson.* **2004**, *168*, 194−201.
(42) Pedersen, J. S. In *Neutrons, X-Rays and Light*; Lindner, P., Zemb, T., Eds.; Elsevier: 2002; Chapter 16, pp 391−420.
(43) Halperin, A. Polymeric Micelles - a Star Model. *Macromolecules* **1987**, *20*, 2943−2946.
(44) Svaneborg, C.; Pedersen, J. S. Form Factors of Block Copolymer Micelles with Excluded-Volume Interactions of the Corona Chains Determined by Monte Carlo Simulations. *Macromolecules* **2002**, *35*, 1028−1037.
(45) Beaucage, G. Approximations Leading to a Unified Exponential/Power-Law Approach to Small-Angle Scattering. *J. Appl. Crystallogr.* **1995**, *28*, 717−728.
(46) Scherrer, P. Bestimmung der Größe und der inneren Struktur von Kolloidteilchen mittels Röntgenstrahlen. *Nachrichten von der Gesellschaft der Wissenschaften zu Göttingen, Mathematisch-Physikalische Klasse* **1918**, 98−100.
(47) Bunn, C. W. The crystal structure of long-chain normal paraffin hydrocarbons. The 'shape' of the CH2 group. *Trans. Faraday Soc.* **1939**, *35*, 482−491.

(48) Yin, L.; Hillmyer, M. A. Disklike Micelles in Water from Polyethylene-Containing Diblock Copolymers. *Macromolecules* **2011**, *44*, 3021−3028.
(49) Fu, D.; Liu, Y.; Gao, X.; Su, Y.; Liu, G.; Wang, D. Binary n-Alkane Mixtures from Total Miscibility to Phase Separation in Microcapsules: Enrichment of Shorter Component in Surface Freezing and Enhanced Stability of Rotator Phases. *J. Phys. Chem. B* **2012**, *116*, 3099−3105.
(50) Halperin, A. Rod-coil copolymers: their aggregation behavior. *Macromolecules* **1990**, *23*, 2724−2731.
(51) Vilgis, T.; Halperin, A. Aggregation of coil-crystalline block copolymers: equilibrium crystallization. *Macromolecules* **1991**, *24*, 2090−2095.
(52) de Gennes, P. G. A second type of phase separation in polymer solutions. *C. R. Acad. Sci.* **1991**, *313*, 1117.
(53) Halperin, A. Compression induced phase transitions in PEO brushes: the n-cluster model. *Eur. Phys. J. B* **1998**, *3*, 359−364.
(54) Dormidontova, E. E. Role of Competitive PEO-Water and Water-Water Hydrogen Bonding in Aqueous Solution PEO Behavior. *Macromolecules* **2002**, *35*, 987−1001.
(55) Maccarini, M.; Briganti, G.; Rucareanu, S.; Lui, X.-D.; Sinibaldi, R.; Sztucki, M.; Lennox, R. B. Characterization of Poly(ethylene oxide)-Capped Gold Nanoparticles in Water by Means of Transmission Electron Microscopy, Thermogravimetric Analysis, Mass Density, and Small Angle Scattering. *J. Phys. Chem. C* **2010**, *114*, 6937−6943.
(56) Grünewald, T. A.; Lassenberger, A.; van Oostrum, P. D. J.; Rennhofer, H.; Zirbs, R.; Capone, B.; Vonderhaid, I.; Amenitsch, H.; Lichtenegger, H. C.; Reimhult, E. Core−Shell Structure of Monodisperse Poly(ethylene glycol)-Grafted Iron Oxide Nanoparticles Studied by Small-Angle X-ray Scattering. *Chem. Mater.* **2015**, *27*, 4763−4771.
(57) Dahal, U.; Wang, Z.; Dormidontova, E. E. Hydration of Spherical PEO-Grafted Gold Nanoparticles: Curvature and Grafting Density Effect. *Macromolecules* **2018**, *51*, 5950−5961.
(58) Sears, V. F. Neutron scattering lengths and cross sections. *Neutron News* **1992**, *3*, 26−37.
(59) Shao-Min, M. A. I.; Booth, C.; Nace, V. M. Specific Volumes of Poly(Oxybutylene) and Poly(Oxyethylene) Dimethyl Ethers in the Liquid State. *Eur. Polym. J.* **1997**, *33*, 991−996.
(60) Lemmon, E. W.; McLinden, M. O.; Friend, D. G. In *NIST Chemistry WebBook, NIST Standard Reference Database Number 69*; Linstrom, P., Mallard, W., Eds.; National Institute of Standards and Technology: Gaithersburg, MD, 2020.
(61) Colby, R. H.; Rubinstein, M. *Polymer Physics*, repr. with corr. ed.; Oxford University Press: Oxford, 2007; pp XI, 440 S.
(62) Lin, S.; He, X.; Li, Y.; Lin, J.; Nose, T. Brownian Molecular Dynamics Simulation on Self-Assembly Behavior of Diblock Copolymers: Influence of Chain Conformation. *J. Phys. Chem. B* **2009**, *113*, 13926−13934.
(63) Zhang, Q.; Clark, C. G.; Wang, M.; Remsen, E. E.; Wooley, K. L. Thermally-Induced (Re)shaping of Core-Shell Nanocrystalline Particles. *Nano Lett.* **2002**, *2*, 1051−1054.
(64) Agrawal, S. K.; Sanabria-DeLong, N.; Tew, G. N.; Bhatia, S. R. Structural Characterization of PLA-PEO-PLA Solutions and Hydrogels: Crystalline vs Amorphous PLA Domains. *Macromolecules* **2008**, *41*, 1774−1784.
(65) Yin, L.; Lodge, T. P.; Hillmyer, M. A. A Stepwise "Micellization−Crystallization" Route to Oblate Ellipsoidal, Cylindrical, and Bilayer Micelles with Polyethylene Cores in Water. *Macromolecules* **2012**, *45*, 9460−9467.
(66) Li, Z.; Liu, R.; Mai, B.; Wang, W.; Wu, Q.; Liang, G.; Gao, H.; Zhu, F. Temperature-induced and crystallization-driven self-assembly of polyethylene-b-poly(ethylene oxide) in solution. *Polymer* **2013**, *54*, 1663−1670.
(67) Liu, R.; Li, Z.-Y.; Mai, B.-Y.; Wu, Q.; Liang, G.-D.; Gao, H.-Y.; Zhu, F.-M. Crystalline-coil diblock copolymers of syndiotactic polypropylene-b- poly(ethylene oxide): synthesis, solution self-assembly, and confined crystallization in nanosized micelle cores. *J. Polym. Res.* **2013**, DOI: 10.1007/s10965-012-0064-6.
(68) Sevgen, E.; Dolejsi, M.; Nealey, P. F.; Hubbell, J. A.; de Pablo, J. J. Nanocrystalline Oligo(ethylene sulfide)-b-poly(ethylene glycol) Micelles: Structure and Stability. *Macromolecules* **2018**, *51*, 9538−9546.
(69) Petzetakis, N.; Walker, D.; Dove, A. P.; O'Reilly, R. K. Crystallization-driven sphere-to-rod transition of poly(lactide)-b-poly(acrylic acid) diblock copolymers: mechanism and kinetics. *Soft Matter* **2012**, *8*, 7408−7414.
(70) Finnegan, J. R.; He, X. M.; Street, S. T. G.; Garcia-Hernandez, J. D.; Hayward, D. W.; Harniman, R. L.; Richardson, R. M.; Whittell, G. R.; Manners, I. Extending the Scope of "Living" Crystallization-Driven Self-Assembly: Well-Defined 1D Micelles and Block Comicelles from Crystallizable Polycarbonate Block Copolymers. *J. Am. Chem. Soc.* **2018**, *140*, 17127−17140.
(71) Noack, S.; Schanzenbach, D.; Koetz, J.; Schlaad, H. Polylactide-Based Amphiphilic Block Copolymers: Crystallization-Induced Self-Assembly and Stereocomplexation. *Macromol. Rapid Commun.* **2019**, *40*, 6.
(72) Xu, J.-T.; Fairclough, J. P. A.; Mai, S.-M.; Ryan, A. J. The effect of architecture on the morphology and crystallization of oxyethylene/oxybutylene block copolymers from micelles in n-hexane. *J. Mater. Chem.* **2003**, *13*, 2740−2748.
(73) Petrov, O.; Furo, I. Curvature-dependent metastability of the solid phase and the freezing-melting hysteresis in pores. *Phys. Rev. E Stat Nonlin Soft Matter Phys.* **2006**, *73*, 011608.
(74) Goebel, A.; Lunkenheimer, K. Interfacial Tension of the Water/n-Alkane Interface. *Langmuir* **1997**, *13*, 369−372.
(75) Zeppieri, S.; Rodriguez, J.; Lopez de Ramos, A. L. Interfacial Tension of Alkane + Water Systems. *J. Chem. Eng. Data* **2001**, *46*, 1086−1088.
(76) Roe, R.-J. Interfacial tension between polymer liquids. *J. Colloid Interface Sci.* **1969**, *31*, 228−235.
(77) Gaines, G. L.; Gaines, G. L. The interfacial tension between n-alkanes and poly(ethylene glycols). *J. Colloid Interface Sci.* **1978**, *63*, 394−398.
(78) Ortony, J. H.; Newcomb, C. J.; Matson, J. B.; Palmer, L. C.; Doan, P. E.; Hoffman, B. M.; Stupp, S. I. Internal dynamics of a supramolecular nanofibre. *Nat. Mater.* **2014**, *13*, 812−6.
(79) Nowacka, A.; Mohr, P. C.; Norrman, J.; Martin, R. W.; Topgaard, D. Polarization transfer solid-state NMR for studying surfactant phase behavior. *Langmuir* **2010**, *26*, 16848−56.
(80) Ferreira, T. M.; Medronho, B.; Martin, R. W.; Topgaard, D. Segmental order parameters in a nonionic surfactant lamellar phase studied with 1H−13C solid-state NMR. *Phys. Chem. Chem. Phys.* **2008**, *10*, 6033−6038.
(81) Nowacka, A.; Bongartz, N. A.; Ollila, O. H. S.; Nylander, T.; Topgaard, D. Signal intensities in 1H−13C CP and INEPT MAS NMR of liquid crystals. *J. Magn. Reson.* **2013**, *230*, 165−175.
(82) Earl, W. L.; VanderHart, D. L. Observations in Solid Polyethylenes by Carbon-13 Nuclear Magnetic Resonance with Magic Angle Sample Spinning. *Macromolecules* **1979**, *12*, 762−767.
(83) Ferreira, T. M.; Topgaard, D.; Ollila, O. H. S. Molecular Conformation and Bilayer Pores in a Nonionic Surfactant Lamellar Phase Studied with 1H−13C Solid-State NMR and Molecular Dynamics Simulations. *Langmuir* **2014**, *30*, 461−469.
(84) Ferreira, T. M.; Coreta-Gomes, F.; Ollila, O. H. S.; Moreno, M. J.; Vaz, W. L. C.; Topgaard, D. Cholesterol and POPC segmental order parameters in lipid membranes: solid state 1H−13C NMR and MD simulation studies. *Phys. Chem. Chem. Phys.* **2013**, *15*, 1976−1989.
(85) Dvinskikh, S. V.; Castro, V.; Sandström, D. Probing segmental order in lipid bilayers at variable hydration levels by amplitude- and phase-modulated cross-polarization NMR. *Phys. Chem. Chem. Phys.* **2005**, *7*, 3255−3257.
(86) Tanford, C.; Nozaki, Y.; Rohde, M. F. Size and shape of globular micelles formed in aqueous solution by n-alkyl polyoxyethylene ethers. *J. Phys. Chem.* **1977**, *81*, 1555−1560.

https://dx.doi.org/10.1021/acs.macromol.0c01936
Macromolecules 2020, 53, 10686−10698

(87) Tomsic, M.; Bester-Rogac, M.; Jamnik, A.; Kunz, W.; Touraud, D.; Bergmann, A.; Glatter, O. Nonionic Surfactant Brij 35 in Water and in Various Simple Alcohols: Structural Investigations by Small-Angle X-ray Scattering and Dynamic Light Scattering. *J. Phys. Chem. B* **2004**, *108*, 7021−7032.
(88) Chen, Z.; Greaves, T. L.; Caruso, R. A.; Drummond, C. J. Amphiphile Micelle Structures in the Protic Ionic Liquid Ethylammonium Nitrate and Water. *J. Phys. Chem. B* **2015**, *119*, 179−191.

https://dx.doi.org/10.1021/acs.macromol.0c01936
Macromolecules 2020, 53, 10686−10698